Aeroelastic-Informed Multi-Objective Optimization of Helicopter Rotor Blades

Muhammad Muneeb Safdar, Apurva Anand, Koushik Marepally, James D. Baeder
University of Maryland, College Park, MD, USA

ABSTRACT

Rotor blade optimization plays a critical role in improving helicopter performance. This study aims to enhance two key metrics: the Figure of Merit (FM) in hover and the Lift-to-Drag ratio (L/D) in forward flight. Traditional high-fidelity methods are accurate but computationally expensive, making them less practical in early-stage design. To address this, we use low-fidelity aerodynamic and structural tools with global optimization methods to efficiently explore the design space. Building on previous work with rigid blade assumptions, this study includes aeroelastic effects to better capture the blade's dynamic behavior. The optimization uses the University of Maryland's Aeromechanical Rotorcraft Analysis Code (UMARC-II) and Genetic Algorithms, allowing for non-linear twist and chord distributions along with spanwise airfoil selection. Two optimization approaches were investigated: with and without airfoil selection parameters. Results show that combining airfoil selection with twist and chord optimization provides the most significant performance gains. Aeroelastic analysis confirms that the optimized blades are structurally feasible, with acceptable modal behavior and deflections in both hover and forward flight.

INTRODUCTION

There is increasing interest in optimizing rotor blades to enhance aerodynamic efficiency. However, this optimization process comes with significant challenges. The design space is vast, multimodal, and often contains local minima, making it difficult to navigate. Additionally, the problem is inherently multi-objective, and the high computational cost of evaluating these objectives adds further complexity. To address these issues, researchers have undertaken various studies to develop effective solutions.

Recent work has advanced rotor blade optimization through a mix of computational and experimental methods. Wilke et al. [1] studied helicopter rotor aerodynamics in hover, combining low-fidelity models with CFD to optimize the HART-II blade's chord and twist. Later work [2] expanded this to include noise reduction during descent, using multi-objective optimization to balance power efficiency and acoustics. For tiltrotors, Jimenez-Garcia et al. [3] showed how adjoint-based CFD optimization could improve performance in both helicopter and airplane modes by adjusting twist and chord distribution. Their gradient-based approach proved efficient, requiring few flow evaluations.

Several studies explored multi-fidelity methods. Leusink et al. [4] combined genetic algorithms with selective CFD runs to optimize hover and forward flight performance at lower computational cost. Similarly, Johnson and Barakos [5] used neural networks with harmonic balance CFD to refine BERP-like tips while maintaining hover efficiency.

Surrogate modeling has grown prominent. Earlier, Zhao et al. [6] trained neural networks on CFD data to optimize turbine blades via genetic algorithms. Other approaches focused on airfoil optimization. Massaro [7] generated Pareto-

Presented at the 51th European Rotorcraft Forum, Venice, Italy , September 9–12, 2025.

optimal airfoils for helicopters using surrogate-assisted methods. Anand et al. [8] recently proposed tandem neural networks to unify high- and low-fidelity optimization. Koushik et al. [9] developed a framework integrating machine learning with CFD to handle airfoil design uncertainties.

We started by using a Linear Inflow model, assuming a rigid blade and bilinear chord and twist distributions [10]. Now, we use nonlinear chord and twist distributions and explore the aeroelastic effects on rotor blade performance.

METHODOLOGY

The section defines the design objectives, flight conditions, trim requirements, and design space to guide the optimization process.

Design Objectives

The problem involves optimizing two main objectives: FM and L/D (Equation 1). The objectives are scaled to prevent bias in the multi-objective optimization.

$$J = w_1 \cdot (FM) + w_2 \cdot \left(\frac{L}{D}\right) \tag{1}$$

Here, w_1 and w_2 are the normalized weights to study the aerodynamic trade-offs, and FM and L/D are given by

$$FM = \frac{C_T^{1.5}}{\sqrt{2} \cdot C_P}, \qquad \frac{L}{D} = \frac{C_L \mu}{C_D \mu + C_Q}$$

Design Space

A HART-II rotor with four rectangular blades and a NACA 23012mod airfoil with a linear twist of -8°/R serves as the baseline. Seven design variables are defined, including inner and outer linear twist, two chord parameters at 0.8 r/R and blade tip, and inner & outer airfoils, with airfoil transition location (Figure 1). The upper and lower bounds are chosen carefully (Table 1). A set of 17 rotorcraft airfoils with various thickness ratios is included in the design space, and constraints are applied to solidity.

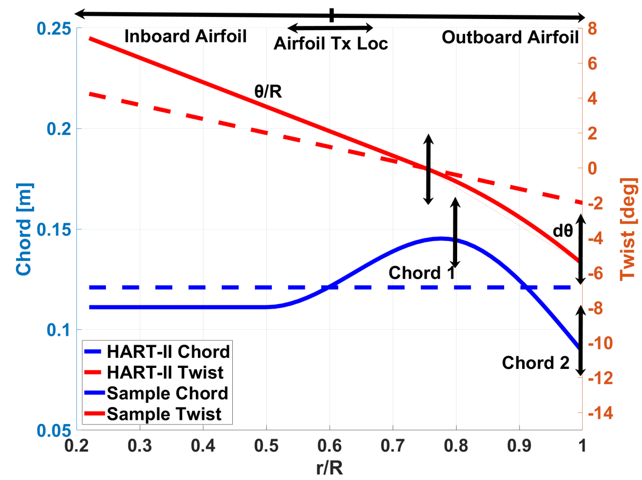

Figure 1: Design variables include 3 twist parameters, 2 chord parameters, and 3 airfoil selection parameters.

Table 1: Design Variables and Bounds

Geometric Variables	Lower bound	Upper bound
Inboard twist rate (deg)	-15	0
Outboard twist rate (deg)	-5	5
Chord 1 (@ 0.8 r/R)	1	1.5
Chord 2 (@ 1.0 r/R)	0.5	1.0
Inboard & Outboard Airfoils	NACA 64-208, SSCA09, SC 1094-R8, SC 1095, VR8, RC3-10, RC4-10, V-23010, VR-7, SC 1012-R8, NACA 0012, NACA 23012, CLARK Y, OA 212, NACA 64-212, VR-12, NACA 0015	
Airfoil transition location	0.3	0.9

Figure 2 shows the first 40 distinct blade designs generated by the genetic algorithm. All designs adhere to three core constraints: zero twist at 75% radius to ensure consistent aerodynamic reference, fixed rotor solidity to maintain disk loading characteristics, and smooth chord distributions achieved through spline interpolation between control points.

Flight and Trim Conditions

The flight and trim conditions for both hover and forward flight are summarized in Table 2. The rotor is trimmed to generate a thrust of 5582 N in both hover and forward flight. In forward flight, a horizontal force of 527 N is generated to balance the drag. The tip Mach number remains constant at 0.641 in both cases. All aerodynamic moments are zeroed out in trim.

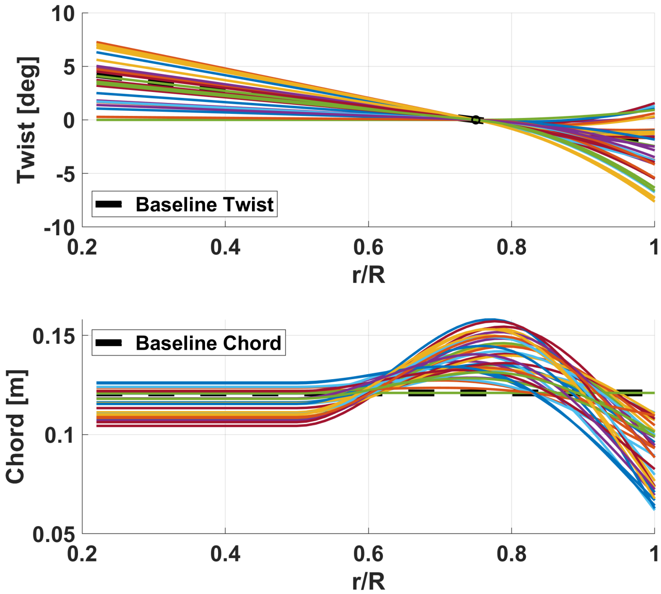

Figure 2: Blade geometry random samples. Top: Twist distributions with baseline HART-II twist. Bottom: Chord distributions with baseline HART-II chord. All designs maintain the same rotor solidity ($\sigma = 0.077$).

Table 2: Flight and Trim Conditions

Flight Condition	Hover	Forward Flight
Thrust (N)	5582	5582
Horizontal Force (N)	0	527
M_{tip}	0.641	0.641
M_∞	–	0.194
M_x	–	0
M_y	–	0

Computational Tool

To ensure an efficient and accurate optimization process, we integrated the University of Maryland Rotorcraft Aeromechanical Analysis Code (UMARC-II) [11] with a Genetic Algorithm. The aeromechanical solver has been validated using experimental data from sources such as the U.S. Army and the Boeing Model 222, showing good agreement in performance predictions [11]. The code employs the Weissinger-L model [12] to estimate the aerodynamic characteristics of rotor blades by predicting lift and drag coefficients based on airfoil properties and flight conditions.

High-fidelity CFD simulations using an enhanced Spalart–Allmaras model, referred to as APGCII-LRe, have been used to generate the airfoil tables [13, 14]. This improved turbulence model enables better prediction of stall onset, more accurate lift estimation in the stall region, and improved drag prediction at low Reynolds numbers. The airfoil tables span Mach numbers from 0.1 to 0.9 and angles of attack from $-180°$ to $180°$, which eliminates the need for extrapolation. These tables are used to optimize airfoil selection for the inner and outer blade spans, as well as to optimize the airfoil transition location along the blade.

UMARC-II provides several inflow models; however, this study employs the linear inflow model, which assumes uniform inflow in hover. The structural coupling is based on one-dimensional Euler–Bernoulli beam theory and includes flapwise and lagwise bending, axial extension, and torsion.

Validation of UMARC-II for Performance and Aeroelastic Response

Figure 3 presents a comparison between the FM predicted by the Linear Inflow model and the experimental data for the HART-II blade. At low blade loading, the model shows close agreement with the experimental results. As C_t/σ increases, deviations appear due to the nonlinear aerodynamic effects. The strong agreement at lower loading levels supports the use of this model for subsequent design optimization.

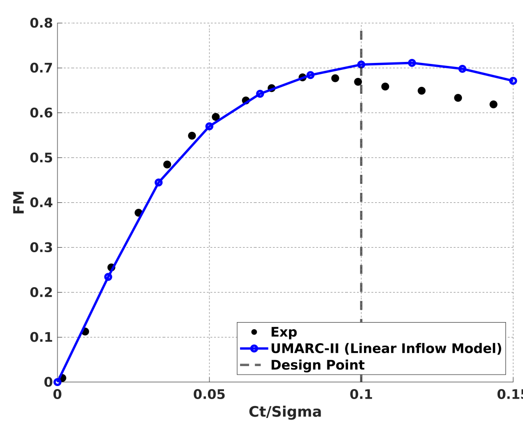

Figure 3: UMARC-II validation for the baseline HART-II blade, closely following experimental data up to a blade loading of 0.08, with minor deviation beyond.

Table 3 presents a frequency comparison between experimental data and UMARC-II predictions for the HART-II blade. The results show good agreement across all modes. The first two modes exhibit a precise match within 1% for the fundamental lag and flap modes (0.78Ω and 1.12Ω, respectively). The maximum difference observed is 4.1% for the second flap mode, while all other modes show differences below 3%, which are most critical for aeroelastic stability. The torsion mode prediction shows a 2.6% difference, which confirms UMARC-II as sufficiently accurate for aeroelastic analysis of rotor blades.

Table 3: Comparison of Frequencies EXP vs UMARC-II

Mode	Exp $\omega/\Omega_{\mathrm{ref}}$	UMARC-II $\omega/\Omega_{\mathrm{ref}}$	Diff %
1st Lag	0.78	0.78	0.8
1st Flap	1.12	1.12	0.8
2nd Lag	2.83	2.81	1.0
2nd Flap	3.85	4.00	4.1
3rd Flap	4.59	4.58	0.3
1st Torsion	5.17	5.03	2.6

Optimizer Details

The design space is non-convex and may contain local minima, so a global optimization method is used. This study uses the Non-dominated Sorting Genetic Algorithm II (NSGA-II), which is suitable for problems with multiple conflicting objectives [15]. Each design is encoded using real-valued variables, and a population of 200 designs evolves over generations. This helps explore a wide range of solutions in fewer generations.

OPTIMIZATION RESULTS

This section presents the findings from two optimization scenarios. The first scenario includes all seven design parameters in the design space, which also includes three airfoil selection parameters. The second scenario excludes airfoil selection parameters and only includes two chord and two twist parameters.

Navigating trade-off

To navigate the trade-off between two objectives, the full optimization scenario is run various weight fractions: one with a maximum weight on FM (using $0.99 \times \mathrm{FM} + 0.01 \times \mathrm{L/D}$), one with a maximum weight on L/D (using $0.01 \times \mathrm{FM} + 0.99 \times \mathrm{L/D}$), and one multi-objective case with higher weight on both. The second optimization scenario (excluding airfoil parameters) is only run for the multi-objective case.

Figure 4 (left) shows the optimization results. Each scatter point represents the best design selected from 200 samples in each generation. In the FM-focused optimization (99% weight on FM), the designs cluster toward high FM values, while in the L/D-focused optimization (99% weight on L/D), the designs cluster toward high L/D values. In the multi-objective case with equal weights, the designs lie between the two extremes, showing a trade-off. Without airfoil selection (second optimization scenario), both FM and L/D values are lower than the full optimization cases. This suggests that airfoil selection contributes significantly to performance improvement.

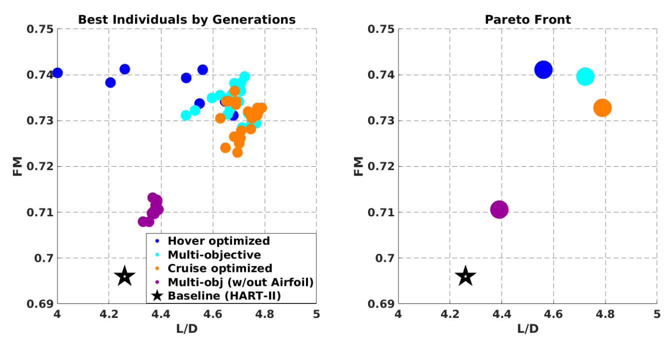

Figure 4: Navigating trade-offs identified three best designs. The optimization without airfoil selection didn't show much improvement.

The Pareto Front (Figure 4 right) shows the best designs from three full optimization cases: hover optimized, cruise optimized, and a multi-objective case with airfoil selection. It also includes the multi-objective case without airfoil selection. The hover-optimized design achieves higher FM but slightly lower L/D. The cruise-optimized case gives better L/D with a small drop in FM. The multi-objective case with airfoil selection offers a balanced trade-off between FM and L/D. Without airfoil selection, both FM and L/D remain low.

Summary of improvements

The trade-offs become clear when looking at percentage changes from the baseline (Figure 5). The hover-optimized blade shows the largest gain in FM, however, its improvement in L/D is modest. With 99% weight on FM, we get a 6.3% FM gain and 7.0 % L/D gain. The multi-objective gives 6.1% FM and 10.85% L/D gain. With 99% weight on L/D, the L/D gain increases to 12.4%, but FM drops to 5.1%. Without airfoil selection, gains drop to 2% FM and 3.1% L/D. This means airfoil choice gives over 60% of the total improvement, more than what chord and twist alone could give.

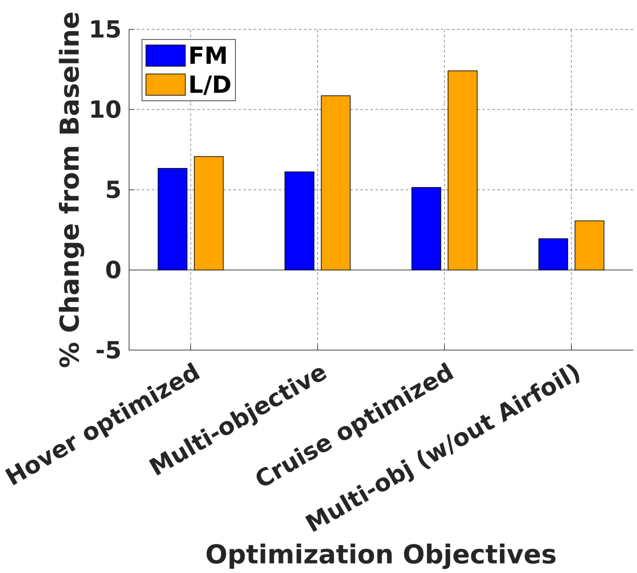

Figure 5: Trade-off between FM and L/D: FM-focused maximizes FM, L/D-focused maximizes L/D, balanced design achieves both. Airfoil selection drives most gains.

Optimized Geometry

Figure 6 shows the twist and chord distributions along the blade span for the baseline, hover-optimized, cruise-optimized, and multi-objective designs. The hover-optimized blade has greater twist near the root and a noticeable increase in chord toward the outer span, which supports high lift generation in hover, along with a reduced tip chord to minimize tip losses. In contrast, the cruise-optimized blade maintains lower twist and a relatively larger tip chord to reduce profile drag during forward flight. The multi-objective blade also uses higher twist than the baseline and exhibits a relatively smooth chord profile.

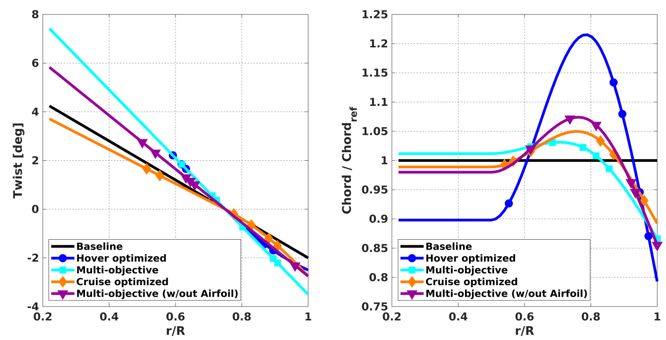

Figure 6: Optimized geometries: Hover favors higher twist and smaller tip chord. Forward flight favors lower twist and relatively larger tip chord. Multi-objective takes higher twist with more uniform chord distribution.

Optimizing Airfoil Selection

Optimizing the airfoil combination for the inboard and outboard regions, along with the transition location, is a key aspect of this study and contributes significantly to improvements in FM and L/D. The optimal airfoil selections for the three optimized designs are given in Table 4, showing distinct combinations selected for each performance objective. The results make physical sense: the inboard section uses thicker airfoils to handle higher loads and provide lift near the hub, while the outboard section uses thinner airfoils to reduce drag and improve efficiency.

Table 4: Optimal Selection of Airfoil for Optimized Designs

Objective	Inner Airfoil	Transition (r/R)	Outer Airfoil
Baseline		NACA 23012mod	
Hover-optimized	NACA 64212	0.674	VR 8
Multi-objective	SC 1095	0.88	VR 8
Cruise-optimized	CLARK Y	0.43	SSCA 09

The multiobjective design selects SC1095 (9.5% thick) from the root to 0.88 r/R and VR8 (8.2% thick) from 0.88 r/R to the tip. This selection matches the flow conditions: the thicker SC1095 handles high lift requirements inboard and outer span where dynamic pressure is modest, while the thinner VR8 reduces drag and improves stall characteristics near tip where Mach numbers are high. For instance, Figure 7 compares the airfoil polars with the baseline NACA23012mod. The VR8 performs best at high Mach numbers (tip Mach = 0.641 in hover, 0.833 in cruise), which makes it ideal for the tip region where most lift is generated. While VR8 excels at high speeds, SC1095 provides better low-Mach performance, justifying its inboard placement.

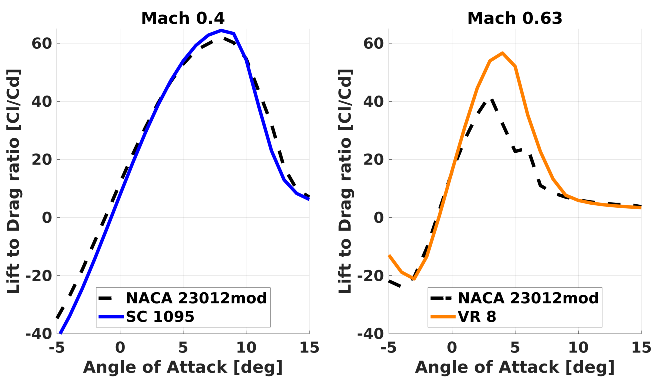

Figure 7: Airfoil VR-8 performs significantly better than NACA 23012mod at higher Mach numbers while SC 1095 performs slightly better than NACA 23012mod at lower mach numbers.

Quantifying the Role of Airfoil Selection

To assess and reiterate the true impact of airfoil selection parameters, we conducted a comparative optimization study. With the same weight fraction between two objectives, we repeated the optimization process with airfoil parameters excluded from the design space.

Figure (8) summarizes the results and reveals two key findings. First, optimizing only twist and chord distributions yielded modest improvements (FM: +2%, L/D: +3.06%) over the baseline. Second, including airfoil selection parameters tripled these gains (FM: +6.1%, L/D: +10.85%), confirming that airfoil characteristics dominate rotor performance. This substantial difference emerged because airfoil shape directly controls boundary layer behavior and stall characteristics, while twist and chord mainly redistribute existing aerodynamic loads. The results emphasize that comprehensive optimization must include airfoil parameters to achieve maximum performance benefits.

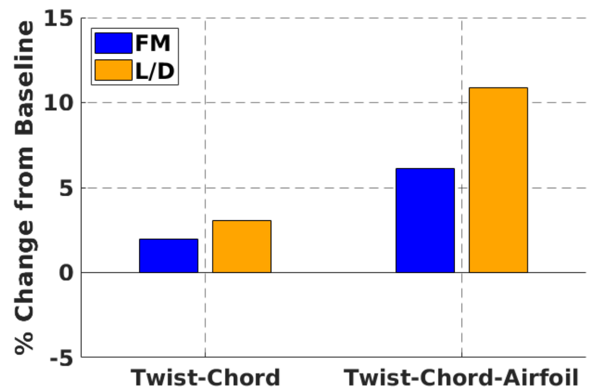

Figure 8: Performance improvements showing 2% FM and 3.1% L/D gains from twist-chord optimization, increasing to 6.1% FM and 10.85% L/D when including airfoil selection.

Control Angle Characteristics

The collective pitch angles in hover are shown in Figure 9. Most designs use a similar hover collective between 8.60–8.70 °, but the multi-objective blade uses a higher value of 9.46 °. This higher collective in hover helps the blade perform better in forward flight. As shown in Figure 10, the multi-objective blade needs a moderate collective angle in forward flight (9.40 °), which is between the baseline (10.25 °) and the hover-optimized design (8.59 °). More importantly, it needs the least lateral cyclic input ($\theta_{1s} = -3.80°$) and longitudinal cyclic input ($\theta_{1c} = 0.37°$), meaning the blade has more balanced loading during forward flight. This reduces the effort needed for roll and pitch trim.

The hover-optimized design achieves 6.3% higher FM than baseline (0.741 vs. 0.697) while maintaining identical collective pitch. The multi-objective optimization strikes a middle ground, delivering

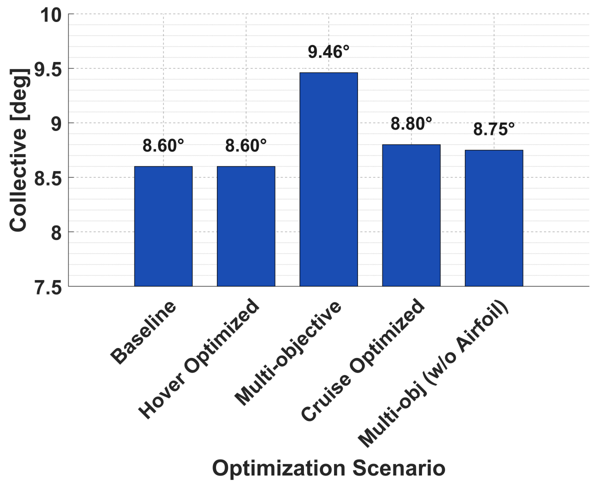

Figure 9: Hover collective pitch (θ_0) comparison across optimization configurations. Multiobjective requires a relatively higher collective.

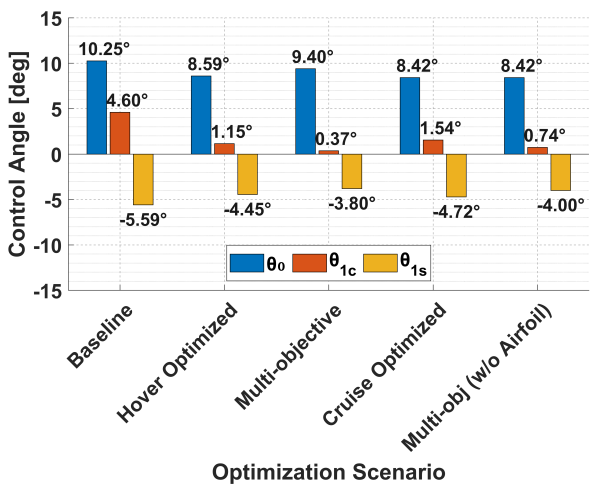

Figure 10: Forward flight control angles showing collective (θ_0), longitudinal cyclic (θ_{1c}), and lateral cyclic (θ_{1s}) inputs. All optimized designs show reduced collective pitch requirements.

94% of the hover performance gain while improving L/D by 11% over baseline, though requiring higher collective pitch in both regimes. All optimized configurations reduce forward flight collective pitch by 15-18% compared to baseline, which suggests more efficient lift distribution across the rotor disk.

Off-design Performance Analysis

The off-design analysis in hover (Figure 11) shows that all designs perform equally well up to a blade loading (CT/σ) of 0.08. At the design point and higher loadings, the hover-optimized and multi-objective blades perform better than the cruise-optimized design, which shows slightly lower FM at higher loadings.

In forward flight (Figure 12), all three blades perform similarly up to a velocity of 50 m/s. At higher speeds, the multi-objective and cruise-optimized blades achieve better L/D, while the hover-optimized blade struggles. Overall, the multi-objective blade offers the best balance between hover and forward flight performance.

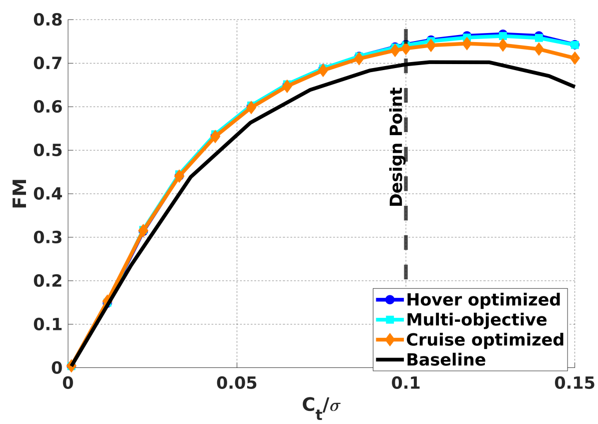

Figure 11: Hover performance showing 0.75 FM as optimal with higher stall margin at high blade loading.

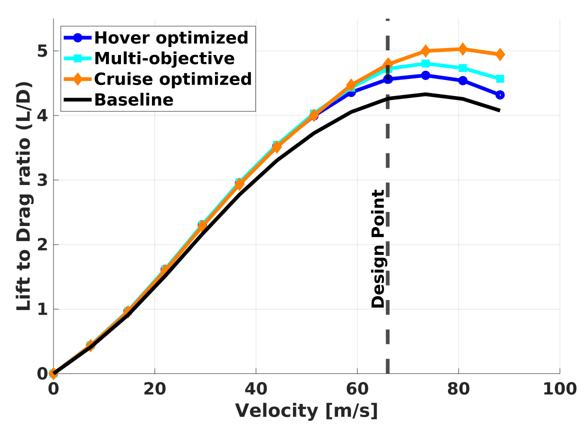

Figure 12: Forward flight performance confirming 0.25 L/D as optimal with better efficiency.

Contribution Analysis of Design Parameters

This analysis examines how individual design parameters contribute to performance improvements compared to the baseline HART-II configuration. Each parameter was varied independently while keeping others at baseline values. The multi-objective optimized twist distribution was assessed with baseline chord and NACA23012mod airfoil, while the optimized chord distribution was evaluated with baseline twist and airfoil. Similarly, the optimal airfoil combination was assessed using baseline twist and chord distributions. Finally, both optimized chord and twist were combined while retaining the baseline airfoil.

The parameter's contributions reveal competing effects on performance metrics. While twist optimization improves both FM (+2.2%) and L/D (+2.3%), chord changes show opposite trends - increasing FM (+0.7%) while decreasing L/D (-4.0%). Airfoil selection alone provides the largest individual FM gain (+5.1%) but still reduces L/D (-1.9%). The combination of optimized twist and chord partially mitigates these trade-offs, achieving +2.9% FM with +0.9% L/D.

The complete optimization integrating all three parameters - twist, chord, and airfoil - achieves the highest performance gains: 6.3% FM increase and 10.8% L/D improvement. These results illustrate that while airfoil selection drives significant FM improvements, its full potential for L/D gains is only realized when properly integrated with compatible twist and chord distributions.

Elastic Versus Rigid Blade Performance

The baseline and three optimized blades were evaluated using rigid blade analysis. Elastic blades mostly achieve higher FM and L/D values compared to their rigid counterparts (Figure 14). This improvement results from the blade's ability to adapt its shape dynamically during rotation. In hover, elastic deformation introduces favorable twist, which reduces induced power losses and increases FM. In forward flight, passive adaptation to asymmetric loading likely improves sectional angles of attack along the span, which enhances L/D.

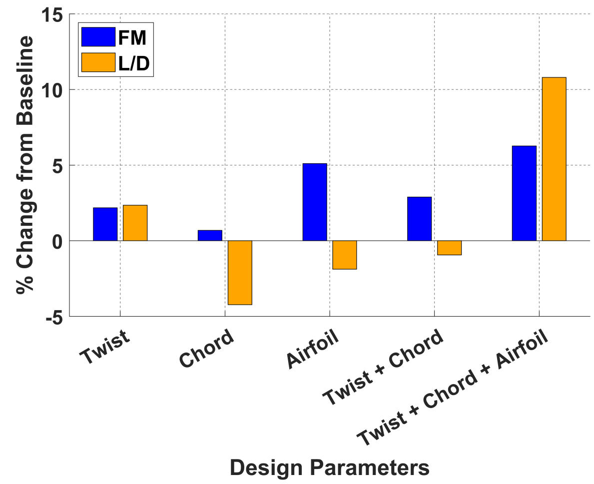

Figure 13: Performance contribution from individual optimized parameter. Twist and chord provide modest improvements, while airfoil changes significantly increase FM but require proper integration with twist and chord to yield maximum improvements (FM: +6.3%, L/D: +10.8%).

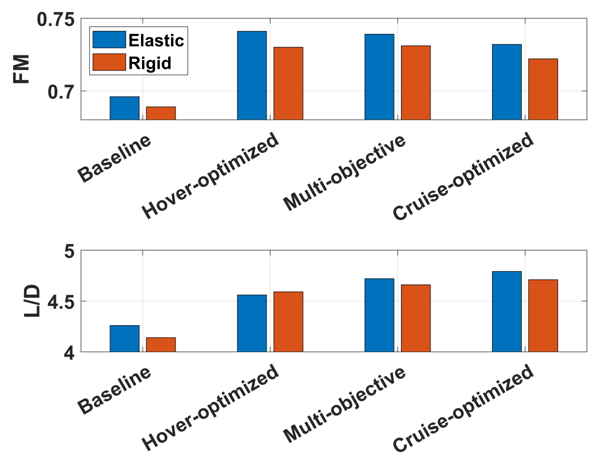

Figure 14: Performance comparison of elastic and rigid blade configurations. Elastic blades mostly outperform rigid ones in both FM and L/D metrics.

AEROELASTIC RESPONSE EVALUATION

This section examines the blade's dynamic behavior under loading using three key analyses: the fan plot characterizes natural frequencies and potential resonances; hover deflections reveal steady-state elastic deformation; and forward flight responses capture cyclic loading effects. The analysis compares the optimized blades with the baseline.

To account for changing blade geometry, the structural properties were scaled based on the local chord distribution. The mass per unit span and axial stiffness were scaled linearly with chord, while torsional stiffness and bending stiffnesses were scaled with the cube of the chord ratio. This simplified scaling captures the first-order effects of geometric changes without performing a full structural optimization. Although more detailed structural modeling could improve accuracy, this approach provides reasonable trends for comparative analysis across different blade designs.

Fan Plot Analysis

Figure 15 compares the natural frequencies of the baseline HART-II blade with those of three optimized designs across a range of rotor speeds. All designs follow a consistent mode sequence up to the first torsional mode, which suggests that optimization mainly affects the stiffness distribution rather than the modal identity. The higher mode frequencies show noticeable drops due to smaller tip chord than the baseline blade, whereas the lower mode frequencies change less significantly (Table 5).

For the hover-optimized blade at design RPM ($\Omega/\Omega_{\text{ref}} = 1$), the first flap and lag modes remain nearly unchanged (within $\pm 0.01\,\omega/\Omega$) because root stiffness dominates these modes. The blade shows lower frequencies in higher modes. This reduction occurs because higher modes are tip-sensitive, and the smaller tip chord (Figure 6) causes stiffness ($EI \propto c^3$) to drop faster than mass ($m \propto c$). The resulting flexibility at the tip, combined with a larger outer span area and aerodynamic loading, enables greater twist and improves hover efficiency if compared with a rigid blade.

The cruise-optimized blade, in contrast, shows slightly higher 1st lag frequency, which reflects stiffer in-plane behavior. Compared to the hover-optimized blade, its relatively larger tip chord mitigates significant drops in higher frequencies (3rd flap: -3.7%, torsion: -5.7% vs baseline).

The cruise-optimized blade shows a +0.9% increase in 1st lag frequency due to its larger inner span area (Table 5). Higher modes see moderate frequency drops (2nd flap: -7.4%, torsion: -5.5%) because the blade's outer is not as larger as the hover-optimized design. This still preserves some tip flexibility for load alleviation while prioritizing cruise efficiency through stiffer inboard structure.

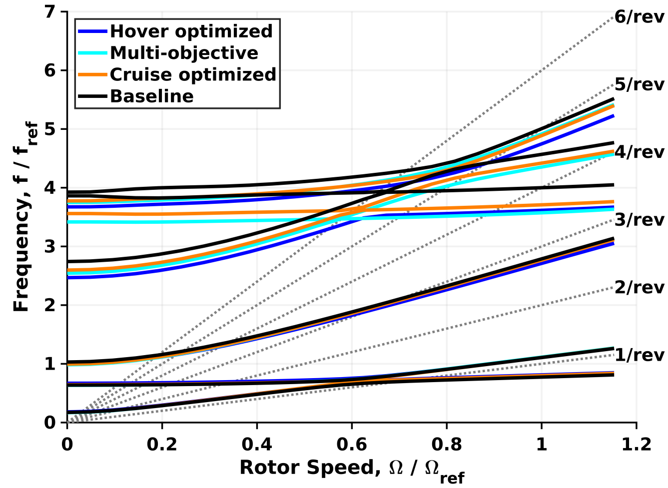

Figure 15: Natural frequency versus rotor speed for baseline and optimized blades. Fundamental modes (1st flap/lag) remain stable near design RPM ($\Omega/\Omega_{\text{ref}} = 1$), while higher modes (2nd/3rd flap, torsion) show reduced frequencies

Table 5: Modal frequencies ($\omega/\Omega_{\text{ref}}$) for baseline and optimized blades

Mode	Baseline	FM Opt.	Multi-Obj.	Cruise Opt.
1st Lag	0.78	0.7811	0.7789	0.7872
1st Flap	1.12	1.1096	1.1251	1.1143
2nd Lag	2.83	2.6961	2.7594	2.7610
2nd Flap	3.85	3.8080	3.5644	3.7012
3rd Flap	4.59	4.3049	4.3662	4.4188
1st Torsion	5.17	4.7023	4.8861	4.8758

Table 6: Comparison of modal frequencies ($\omega/\Omega_{\text{ref}}$) between baseline and multi-objective optimized blades.

Mode	Baseline	Multi-Obj.	% Change
1st Lag	0.78	0.7789	−0.14%
1st Flap	1.12	1.1251	+0.46%
2nd Lag	2.83	2.7594	−2.49%
2nd Flap	3.85	3.5644	−7.43%
3rd Flap	4.59	4.3662	−4.88%
1st Torsion	5.17	4.8861	−5.49%

The natural frequencies of the multi-objective optimized blade were compared with the baseline blade for the hover condition (Table 6). The first lag and flap modes showed very small changes, with the first lag mode decreasing by 0.14% and the first flap increasing slightly by 0.46%. Higher modes, such as the second flap, third flap, and torsion, showed larger reductions. In particular, the second flap mode dropped by about 7.4% and the torsional frequency decreased by 5.5%. This shift in frequencies indicates that the optimized blade became more flexible in higher modes, which is a trade-off resulting from changes in mass and stiffness distribution to improve aerodynamic performance.

Spanwise Blade Deformation in Hover

Figure 16 shows the spanwise distribution of flapwise, lagwise, and torsional deflections in hover for the baseline and optimized blades.

The flapwise deflection increases from root to tip in all cases, with all three optimized blades showing greater deflections than the baseline. This can be attributed to the larger blade area around $0.6 \leq r/R \leq 0.85$, which results in higher aerodynamic loading in the outer span. The hover-optimized blade exhibits a 17% larger peak-to-peak flapwise deflection (0.0726 m) compared to the baseline (0.0618 m), despite its higher inboard twist rate (-14° vs -8°). This increase results from reduced chord at both the root and tip, which lowers flapwise stiffness (evident in the lower 2nd and 3rd flap frequencies in Table 5), while the increased mid-span chord enhances lift generation. The increased deflections in the multi-objective and cruise-optimized blades are also influenced by slightly lower higher-mode frequencies due to reduced tip stiffness (see Table 5).

Lagwise deflections remain small but show variation due to changes in in-plane stiffness and aerodynamic drag distribution. The cruise-optimized blade shows nearly the same deflection as the baseline due to its more uniform chord distribution. The hover-optimized blade shows the highest deflection due to a larger outer span area and the associated drag. The multi-objective blade shows intermediate deflection due to its relatively uniform chord distribution.

Torsional deflections reveal the most noticeable differences. The cruise-optimized blade exhibits the highest torsional deflection, consistent with its reduced torsional stiffness and frequency (4.8758 vs. 5.17 for the baseline in Table 5). In contrast, the multi-objective blade shows the smallest torsional deflection despite having a high geometric twist. This is likely due to its larger inboard area up to $r/R = 0.8$, which increases stiffness as also evident by higher 1st torsion frequency. The hover-optimized blade shows intermediate torsional deflection due to its larger outer span area and the associated stiffness.

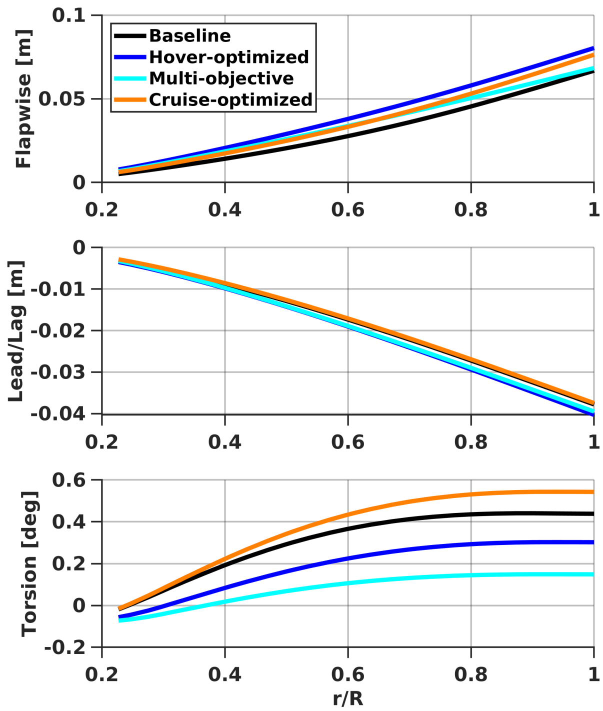

Figure 16: Spanwise deflection in hover: Out-of-plane blade deflection shows larger upward bending with highest in the hover-optimized blade. In-plane deflection shows higher backward bending in the hover-optimized and multi-objective optimized case. Torsional deflection is reduced and more stable in the multi-objective optimized blade.

Tip Deflection Behavior in Forward Flight

The tip deflection behavior of rotor blades in forward flight is analyzed using time histories of tip deflections (Figure 17) and peak-to-peak deflection magnitudes at the blade tip (Table 7).

The Hover-optimized and Multi-objective blades exhibit larger flapwise deflections and substantially higher torsional deflections compared to the baseline, consistent with their higher inboard twist rate

($-14°$). The Hover-optimized blade features lower tip twist than the Multi-objective blade, which alleviates the torsional tendency. The Cruise-optimized blade shows flapwise and torsional behavior closer to the baseline due to its lower twist rate ($-7°$). All configurations maintain similar lead-lag deflection magnitudes with peaks shifted a bit earlier than the baseline. This suggests that twist and chord redistribution primarily influence flapwise and torsional responses.

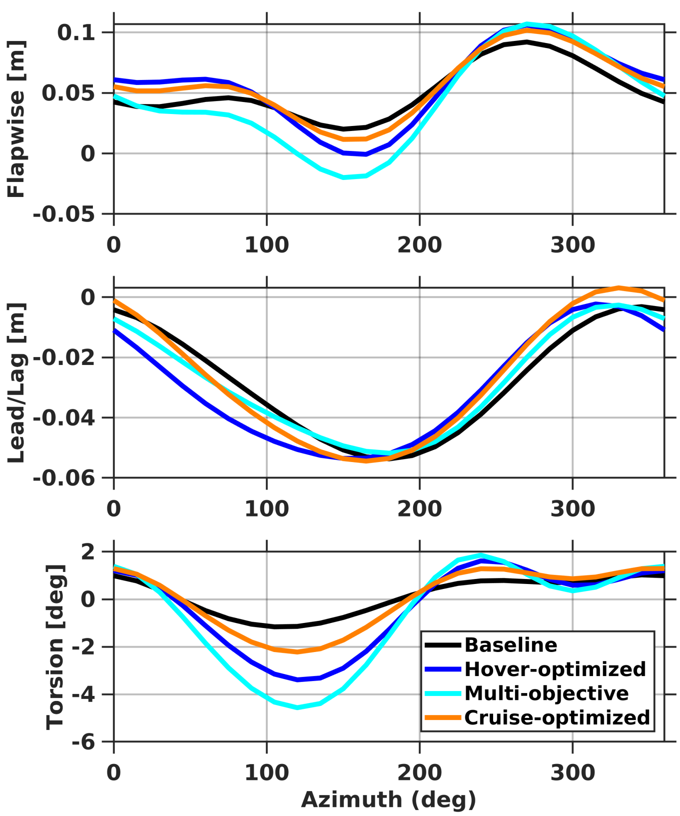

Figure 17: Tip deflections in forward flight: Larger twist in Hover-optimized and Multi-objective blades correlates with higher torsional and flapwise peak-to-peak deflections. The Cruise-optimized blade shows relatively lower peak-to-peak deflections, though still higher than the baseline.

Azimuthal and Spanwise Deflection Behavior of the Multi-Objective Blade in Forward Flight

To further investigate rotor deformation in forward flight, the azimuth–spanwise deflection characteristics of the Multi-objective blade are compared with the baseline configuration.

Table 7: Peak-to-peak tip deflection characteristics for different blade configurations

Configuration	Flapwise (m)	Lead-Lag (m)	Torsional (°)
Baseline	0.0720	0.0506	2.1857
Hover-optimized	0.1069	0.0513	5.0078
Multi-objective	0.1269	0.0492	6.4224
Cruise-optimized	0.0902	0.0575	3.5145

In flapwise bending (Figure 18), both the baseline and Multi-objective blades exhibit peak deflections near 180° azimuth, corresponding to the region of highest lift. However, the optimized blade shows a slightly delayed and stronger peak, beginning around 145° and extending to 250°. This increase and shift in the peak are likely caused by the higher built-in twist and increased aerodynamic loading near the tip, resulting from the optimized chord and twist distribution. These changes affect local angles of attack and delay the onset of maximum lift-induced bending.

Lagwise deflections are primarily governed by in-plane aerodynamic and inertial forces (Figure 19). For the baseline blade, peak lag deflection occurs near 85° azimuth on the advancing side where drag forces are typically stronger (Figure 19). The optimized blade shows a slightly earlier and lower peak, around 78°, which suggests improved chord distribution and airfoil selection. This may also indicate an increase in in-plane stiffness, which contributes to reduced lagwise bending amplitude.

Torsional deflections exhibit the most significant differences between blade configurations (Figure 20). The baseline blade displays a relatively uniform torsional response along the span with modest variation, likely due to its lower built-in twist and higher torsional rigidity. In contrast, the multi-objective optimized blade experiences more pronounced torsional deflection, with a maximum of approximately $+1°$ at 150° azimuth and a large negative twist rate of $-42°$ near 45° azimuth at the tip. These variations stem from the interaction of larger geometric twist and reduced torsional stiffness with rapidly varying aerodynamic moments, especially in the retreating-to-advancing transition.

While the flapwise and lagwise deflection patterns

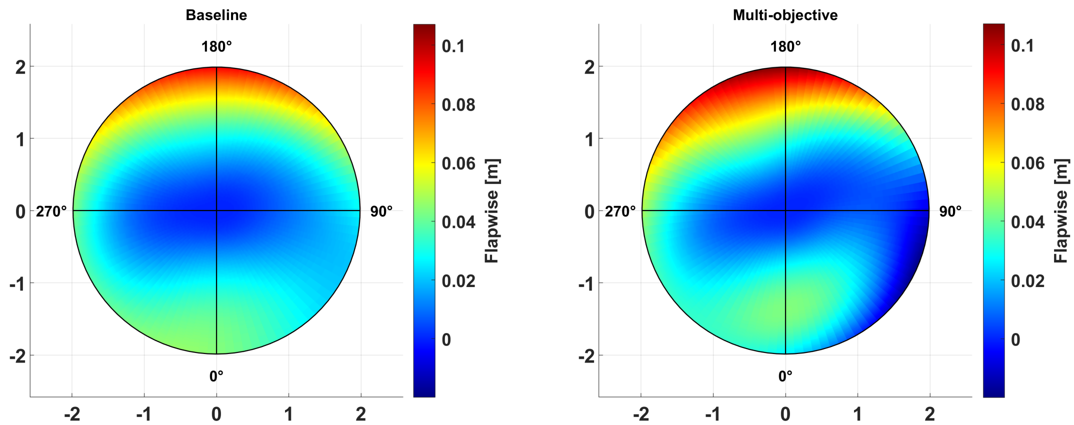

Figure 18: Flapwise deflection shows larger flapping amplitudes for multi-objective optimized blade due to $-14°$ twist rate versus baseline $-8°$, with delayed peak (190° vs 180°).

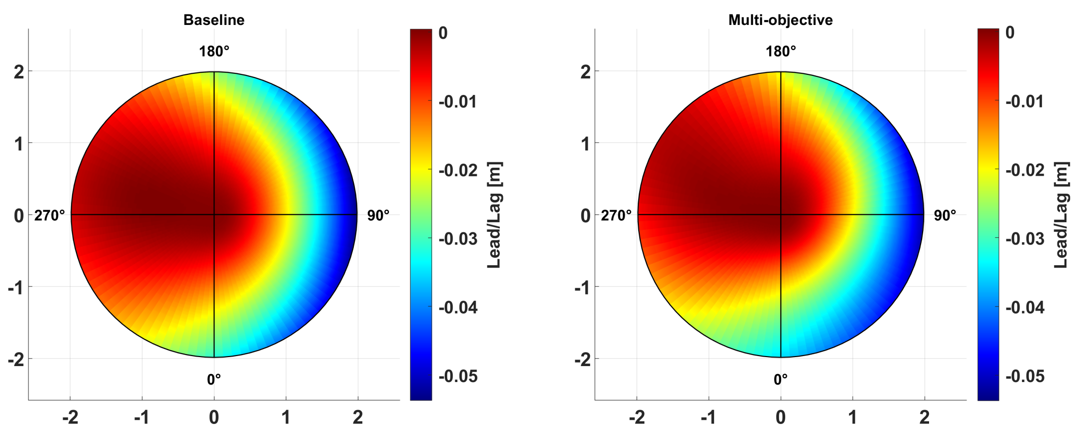

Figure 19: The optimized blade shows a slightly earlier and lower peak, around 78°, which suggests improved chord distribution and airfoil selection.

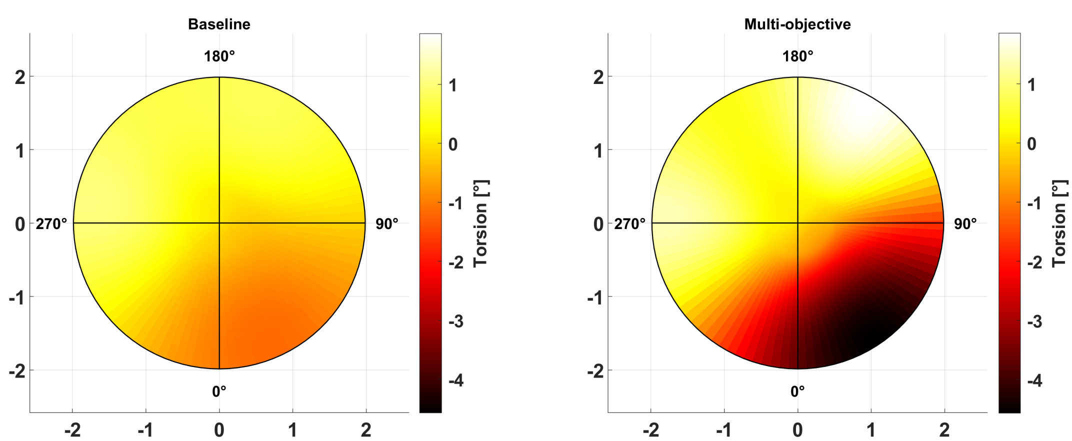

Figure 20: Torsional response shows -4.2° torsion peak at 45° azimuth in multi-objective design most likely due to higher tip twist, smaller chord and tip stiffness reduction.

remain qualitatively consistent with the baseline, the enhanced torsional dynamics highlight the effectiveness of structural tailoring in managing aerodynamic loads and improving aeroelastic performance.

Among the three optimized blade designs (hover-optimized, multi-objective, and cruise-optimized), the cruise-optimized shows the most favorable aeroelastic behavior. It exhibits lower flapwise and torsional deflections compared to the other two designs, while achieving the highest (L/D) and maintaining a competitive FM). Furthermore, its natural frequency distribution is better aligned with dynamic stability requirements. Taken together, this makes the cruise-optimized blade the most practical choice.

CONCLUSIONS AND FUTURE WORK

This study presents an efficient framework for optimizing rotor blades to improve performance in both hover and forward flight. The design process accounts for blade elasticity, and all aeroelastic evaluations are performed using UMARC-II. Starting from the HART-II baseline, the optimization includes airfoil selection, as well as twist and chord distributions.

Two optimization strategies were explored: one with airfoil selection parameters and one without. Optimizing chord, twist and airfoil selection parameters in the design space, led to significant improvements. The multi-objective design with optimizing airfoil selection achieved a 6.1% improvement in FM and a 10.8% improvement in L/D compared to the baseline. In contrast, the design without airfoil selection achieved only a 2% improvement in FM and 3.1% in L/D. The contribution of each optimized design parameter toward the overall performance gain further showed that the full benefit is realized only when airfoil selection is combined with twist and chord optimization.

Aeroelastic analysis showed that fundamental modes (1st flap and lag) remained stable, while higher-mode frequencies decreased in blades with reduced tip chord. These changes introduced more flexibility, especially near the tip, which helped accommodate aerodynamic loads. In hover, spanwise deflection patterns revealed increased flapwise bending in optimized blades due to higher outer span loading. Lagwise deflections showed moderate in-plane bending near mid-span, consistent with increased chord area and drag in outer span region. Torsional deflections were smaller and more stable in optimized blades due to the built-in geometric twist, which reduced the need for elastic twist. In forward flight, the optimized blade showed relatively higher and delayed flap deflection due to higher twist and tip loading. Lag deflection was reduced and peaked earlier. Torsional deflections increased to adapt to the redistributed aerodynamic loads.

Among hover-optimized, multi-objective, and cruise-optimized blades, the cruise-optimized design proves most practical, showing lower deflections, highest L/D, competitive FM with well distributed natural frequencies.

Future work will focus on high-fidelity CFD validation of the optimized geometries to confirm aerodynamic gains and understand flow behavior. Additionally, instead of selecting from a predefined airfoil set, we plan to integrate an in-house surrogate model [16] that predicts polars of aerodynamic coefficients based on airfoil geometry and Mach numbers. This will allow greater flexibility and precision in airfoil design. An inverse design Artificial Neural Network framework [17] would be used to further enhance the performance of optimized airfoils. Finally, acoustic performance will be included in the optimization objectives to evaluate trade-offs between noise reduction and aerodynamic efficiency for a more comprehensive rotor design.

*

REFERENCES

[1] G. Wilke, J. Bailly, K. Kimura, and Y. Tanabe. "JAXA-ONERA-DLR cooperation: results from rotor optimization in hover". In: *CEAS Aeronautical Journal* 13 (2022), pp. 313–333. DOI: 10.1007/s13272-021-00512-y.

[2] G. Wilke. "Quieter and Greener rotorcraft: concurrent aerodynamic and acoustic optimization". In: *CEAS Aeronautical Journal* 12 (2021), pp. 495–508. DOI: 10.1007/s13272-021-00513-x.

[3] A. Jimenez-Garcia, M. Biava, G. N. Barakos, K. D. Baverstock, S. Gates, and P. Mullen. "Tiltrotor CFD Part II: Aerodynamic Optimisation of Tiltrotor Blades". In: *The Aeronautical Journal* (2017). DOI: 10.1017/aer.2017.37.

[4] D. Leusink, D. Alfano, and P. Cinnella. "Multi-Fidelity Optimization Strategy for the Industrial Aerodynamic Design of Helicopter Rotor Blades". In: *Aerospace Science and Technology* 42 (2015), pp. 136–147. DOI: 10.1016/j.ast.2015.01.005.

[5] C. S. Johnson and G. N. Barakos. "A Framework for the Optimisation of a BERP-like Blade". In: *University of Liverpool and University of Glasgow Research* (2013).

[6] H. Zhao, S. Wang, W. Han, and G. Feng. "Aerodynamic Design by Jointly Applying S2 Flow Surface Calculations and Modern Optimization Methods on Multistage Axial Turbines". In: *Frontiers of Energy and Power Engineering in China Journal* 2.1 (2008), pp. 93–98. DOI: 10.1007/s11708-008-0007-4.

[7] A. Massaro and E. Benini. "Multi-Objective Optimization of Helicopter Airfoils Using Surrogate-Assisted Memetic Algorithms". In: *Journal of Aircraft* 49.2 (2012), pp. 375–383.

[8] A. Anand, K. Marepally, M. M. Safdar, B. Lee, and J. D. Baeder. "Generalizable Deep Learning Module for Rotorcraft Inverse Design Applications". In: *AIAA SCITECH 2024 Forum*. 2024. DOI: 10.2514/6.2024-0460.

[9] M. M. Safdar, A. Anand, K. Marepally, B. Lee, and J. D. Baeder. "A Surrogate Modeling Framework for Airfoil Design and Optimization". In: *AIAA Scitech 2024 Forum*. 2024. DOI: 10.2514/6.2024-0458.

[10] M. M. Safdar, A. Anand, K. Marepally, and J. D. Baeder. "Navigating Aerodynamic Trade-Offs: Multi-Objective Optimization of Helicopter Rotor Blade Using an Evolutionary Algorithm". In: *AIAA SciTech Forum*. 2025. DOI: 10.2514/6.2025-0017.

[11] S. Gul. "A Modern Aeromechanical Analysis of Hingeless Hub Tiltrotors with Model- and Full-Scale Wind Tunnel Validation". PhD thesis. Aerospace Engineering, UMD, 2022.

[12] A. Weissinger. "The Aerodynamics of Rotor Blades". In: *Journal of Aeronautical Science* 2 (1935), pp. 250–259.

[13] M. M. Safdar, A. Anand, and J. D. Baeder. "Functional Correction to Spalart-Allmaras Turbulence Model Using Field Inversion and Data Mining: A Novel Approach". In: *AIAA Aviation 2024 Forum*. 2024. DOI: 10.2514/6.2024-4087.

[14] M. M. Safdar. "Enhanced Spalart-Allmaras Turbulence Model: Unified Corrections for Adverse Pressure Gradient and Low Reynolds Number Effects". In: *AIAA Aviation Forum*. 2025. DOI: 10.2514/6.2025-3176.

[15] K Deb, A Pratap, S Agarwal, and T Meyarivan. "A fast and elitist multiobjective genetic algorithm: NSGA-II". In: *Trans. Evol. Comp* 6.2 (2002), pp. 182–197. DOI: 10.1109/4235.996017.

[16] A. Anand, K. Marepally, M. M. Safdar, B. Lee, and J. D. Baeder. "Generalizable Deep Learning Module for Rotorcraft Inverse Design Applications". In: *AIAA 2024-0460, Session: Special Session: Applied Surrogate Modeling III*. 2024. DOI: 10.2514/6.2024-0460.

[17] A. Anand, K. Marepally, M. M. Safdar, B. Lee, and J. D. Baeder. "A Novel Approach to Inverse Design of Wind Turbine Airfoils Using Tandem Neural Networks". In: *Wind Energy* 27.9 (Sept. 2024), pp. 900–921.